Research Article

Meng Han*, Chuwei Zhou, Vadim V. Silberschmidt, Xindong Ma, Mao Liu, Wenan Jiang and Qinsheng Bi

Oblique penetration mechanism of hybrid composite laminates

https://doi.org/10.1515/secm-2021-0054
received May 07, 2021; accepted September 24, 2021

Abstract: Hybrid fiber composites are widely used to improve the anti-penetration performance. Carbon/Kevlar hybrid composites are used in aircrafts and safety devices, thanks to the strong toughness of Kevlar fibers and high strength of carbon fibers. In the present work, the contact force of hybrid composites under oblique impact is derived. The viscoelastic constitutive model of Kevlar layer is investigated and the dissipation energies of composites for different high velocity oblique impacts are simulated. The results show that hybrid composites have good bullet-proof performance, the contact forces are fluctuant in short time and the frictional dissipation energy allows us to prevent penetration.

Keywords: contact force, dissipation energy, hybrid composite, oblique penetration

1 Introduction

Composite materials are widely used in the aircraft structures, which should be of certain impedance capability for a variety of complex loads. Due to the high specific strength, low weight, and good resistance, hybrid composites have been widely used [1]. In particular, their behavior under high impact loads is paid more attention in aerospace engineering. There are a lot of experimental and simulated studies in the literature on hybrid composites under high velocity impact tests. Heydari et al. studied, both experimentally and numerically, the elastic modulus of polymers reinforced with nanoclay [2], but the interfacial debonding between matrix and nanoclay was not considered. Xu et al. [3] studied the high velocity penetration resistance of carbon fiber reinforced polymeric (CFRP) and CFRP_aluminum laminates through experimental tests and showed that the carbon fiber reinforced aluminum laminate (CRALL) targets had better penetration resistance to the three shapes of nose projectiles than CFRP in terms of both ballistic limits and energy absorption performance, due to the strain rate hardening effect. Sayer et al. studied the impact response and damage process of hybrid composite plates under low velocity impact [1]. Naresh et al. experimentally and theoretically studied the tensile properties of glass/epoxy, carbon/epoxy, and hybrid (glass-carbon/epoxy) composites [4] influenced by strain rate and showed that failure strain changed with the increase in strain rate. Tirillo et al. investigated the effect of basalt fiber hybridization in carbon/epoxy laminates on high velocity impacts through experiments [5] and showed that the stacking sequence affected the ballistic limit, with the intercalated $[(B_2/C_2)_3/B_2/C]_S$ configuration exhibiting the highest value among all hybrids. Xie et al. [6] described the correlations between the mechanical performances and different impact factors on the structural integrity of advanced carbon–carbon composites for high temperature through impact tests on heated composite samples. Tao et al. [7] proposed a method to identify crack tip elements with a virtual fatigue damage variable and simulated the delamination in composite materials under fatigue loads using extended cohesive interface elements. Yao et al. [8] experimentally and numerically investigated the successive impact response and accumulated damage of fiber metal laminates under oblique successive impacts. Srivatsava et al. [9] assessed experimentally the dynamic mechanical properties of carbon, Kevlar, hybrid, and sandwich configuration composites and

* **Corresponding author: Meng Han,** Faculty of Civil Engineering and Mechanics, Jiangsu University, Zhenjiang 212013, Jiangsu Province, People's Republic of China, e-mail: hanm@ujs.edu.cn
Chuwei Zhou: State Key Laboratory of Mechanics and Control of Mechanical Structures, Nanjing University of Aeronautics and Astronautics, Nanjing 210001, Jiangsu Province, People's Republic of China
Vadim V. Silberschmidt: Wolfson School of Mechanical, Electrical and Manufacturing Engineering, Loughborough University, Loughborough, Leicestershire LE11 3TU, United Kingdom
Xindong Ma, Mao Liu, Wenan Jiang, Qinsheng Bi: Faculty of Civil Engineering and Mechanics, Jiangsu University, Zhenjiang 212013, Jiangsu Province, People's Republic of China

showed that sandwich and hybrid fiber composites exhibited superior damping properties at higher frequencies. Woo and Kim [10] showed that the high strain rate induced failure characteristics in a carbon/Kevlar hybrid composite subjected to high strain rate compressive loading using a novel SHPB-AE coupled test.

Only a few theoretical research studies on the hybrid composite under the high velocity impact are available in the literature. Sanchez-galvez et al. presented an improved analytical model which considered oblique impact [11], which is able to predict with high accuracy both the ballistic limit and the residual velocity. The analytical model has been worked to analyze also the impact on hybrid composite material targets [12].

Oblique impact is common in the flight accidents, such as bird impact, hail impact, and aero-engine fan released blade impact. Carbon/Kevlar hybrid composite is the optimal material with impact resistance potential, and the research on high velocity oblique impact over 200 m/s is scarce. In this article, the contact force of hybrid composites under oblique impact is derived based on the cavity expansion theory, and the strain rate-dependent property of Kevlar, the stress distribution, damage dissipation, and frictional dissipation energies are simulated, in order to reveal the mechanism of oblique penetration and provide suggestions for the design of protective equipment.

2 Contact force analysis of hybrid composite

High velocity impact is a penetration process, so the cavity expansion theory [13,14] needs to be employed to analysis. The normal stress σ_n of projectile nose [15], which is penetrating into the target, is equal to the radial stress σ_r:

$$\sigma_n = \sigma_r. \tag{1}$$

The frictional stress σ_τ is obtained by:

$$\sigma_\tau = \mu\sigma_r. \tag{2}$$

The normal resistance σ_{zn} and tangential one $\sigma_{z\tau}$ can be calculated as:

$$\begin{cases} \sigma_{zn} = \sigma_r \cos\theta + \sigma_t \sin\theta = \sigma_r(\cos\theta + \mu\sin\theta), \\ \sigma_{z\tau} = \sigma_r \sin\theta - \sigma_t \cos\theta = \sigma_r(\sin\theta - \mu\cos\theta), \end{cases} \tag{3}$$

where μ is the sliding friction coefficient, θ is the angle between the curvature radius of tip and dotted line (d) paralleled with axial direction of projectile, and α is the angle between axis of projectile and horizontal plane of target, as shown in Figure 1.

The normal force and axial resistance force of the projectile nose can be obtained as [16]:

$$\begin{cases} \mathrm{d}F_n = 2\pi s^2(\sin\theta - \sin\theta_0)\sigma_n \mathrm{d}\theta, \\ \mathrm{d}F_z = 2\pi s^2(\sin\theta - \sin\theta_0)\sigma_z \mathrm{d}\theta, \\ \mathrm{d}F_{z\tau} = 2\pi s^2(\sin\theta - \sin\theta_0)\sigma_{z\tau} \mathrm{d}\theta, \end{cases} \tag{4}$$

where θ_0 is the angle between the line (oa) and the dotted line (d) paralleled with axis of the projectile, as shown in Figure 1; point "o" is the tip node of projectile, point "a" is the intersection node between local reference system of projectile and surface of target, and "s" is the length of line (oa).

According to equations (1), (3), and (4), the following equations can be obtained:

$$\begin{cases} \mathrm{d}F_n = 2\pi s^2\sigma_r(\sin\theta - \sin\theta_0)\mathrm{d}\theta, \\ \mathrm{d}F_z = 2\pi s^2\sigma_r(\sin\theta - \sin\theta_0)(\cos\theta + \mu\sin\theta)\mathrm{d}\theta, \\ \mathrm{d}F_{z\tau} = 2\pi s^2\sigma_r(\sin\theta - \sin\theta_0)(\sin\theta - \mu\cos\theta)\mathrm{d}\theta. \end{cases} \tag{5}$$

So the force components in the global coordinate system of target are calculated as:

$$\begin{cases} \mathrm{d}F_{z'} = \mathrm{d}F_z \sin\alpha + \mathrm{d}F_{z\tau}\cos\alpha, \\ \mathrm{d}F_{x'} = \mathrm{d}F_z \cos\alpha - \mathrm{d}F_{z\tau}\sin\alpha. \end{cases} \tag{6}$$

The radial stress on the surface of the projectile nose can be calculated with the velocity and angle as follows [17]:

$$\sigma_r(V_z,\theta)/Y = \frac{2}{3}\left[1 + \left(\frac{2E}{3Y}\right)^n \int_0^{1-(3Y-2E)} \frac{(-\ln x)^n}{1-x}\right] + \frac{3}{2}[(\rho_t/Y)^{1/2}V_z\cos\theta]^2, \tag{7}$$

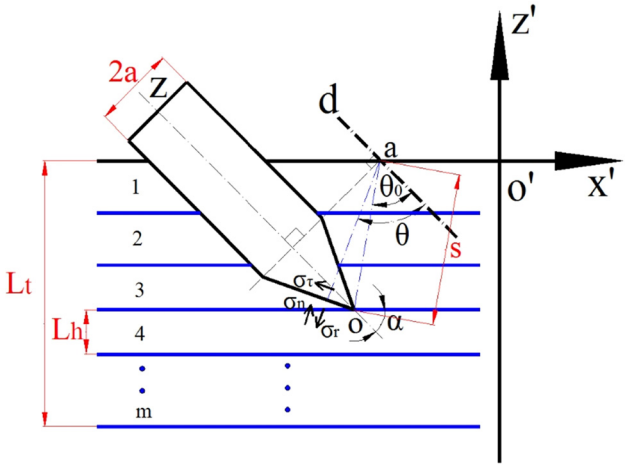

Figure 1: Penetration diagram of hybrid fiber laminates.

where ρ_t and Y are the density of plate material and the yield strength of plate material, respectively, A and B are constants related to the characteristics of the plate materials, and V_z is the impact velocity of the projectile.

According to equations (5)–(7), the contact force of target can be obtained as:

$$\begin{cases} F_{z'} = 2\pi s^2 \left(\begin{aligned} &\sin\alpha \int_{\theta_i}^{\theta_j} (\sin\theta - \sin\theta_0)(\cos\theta + \mu\sin\theta)(AY + B\rho_t V_z^2 \cos^2\theta)\mathrm{d}\theta \\ &+ \cos\alpha \int_{\theta_i}^{\theta_j} (\sin\theta - \sin\theta_0)(\sin\theta - \mu\cos\theta)(AY + B\rho_t V_z^2 \cos^2\theta)\mathrm{d}\theta \end{aligned} \right) \\ F_{x'} = 2\pi s^2 \left(\begin{aligned} &\cos\alpha \int_{\theta_i}^{\theta_j} (\sin\theta - \sin\theta_0)(\cos\theta + \mu\sin\theta)(AY + B\rho_t V_z^2 \cos^2\theta)\mathrm{d}\theta \\ &- \sin\alpha \int_{\theta_i}^{\theta_j} (\sin\theta - \sin\theta_0)(\sin\theta - \mu\cos\theta)(AY + B\rho_t V_z^2 \cos^2\theta)\mathrm{d}\theta \end{aligned} \right) \end{cases}. \tag{8}$$

Because the hybrid composite plate has lots of layers with different fibers, the penetration process can be considered to contain different stages.

At the initial stage, the projectile has not contacted the target, $F_{z'} = F_{x'} = 0$. When the projectile nose contacts the top surface of the target, it is supposed that the effective displacement z is the initial value zero. The total thickness and the number of layers of target are L_t and m, respectively.

(1) Before the nose wholly penetrates into the target ($0 < z\sin\alpha \le L_h$), the contact force can be calculated as:

$$\begin{cases} F_{z'} = 2\pi s^2 \left(\begin{aligned} &\sin\alpha \sum_{k=1}^{n} \left[\int_{\theta_{ki}}^{\theta_{kj}} (\sin\theta - \sin\theta_0)(\cos\theta + \mu\sin\theta)(A_k Y_k + B_k\rho_{tk} V_{zk}^2 \cos^2\theta)\mathrm{d}\theta \right] \\ &+ \cos\alpha \sum_{k=1}^{n} \left[\int_{\theta_{ki}}^{\theta_{kj}} (\sin\theta - \sin\theta_0)(\sin\theta - \mu\cos\theta)(A_k Y_k + B_k\rho_{tk} V_{zk}^2 \cos^2\theta)\mathrm{d}\theta \right] \end{aligned} \right) \\ F_{x'} = 2\pi s^2 \left(\begin{aligned} &\cos\alpha \sum_{k=1}^{n} \left[\int_{\theta_{ki}}^{\theta_{kj}} (\sin\theta - \sin\theta_0)(\cos\theta + \mu\sin\theta)(A_k Y_k + B_k\rho_{tk} V_{zk}^2 \cos^2\theta)\mathrm{d}\theta \right] \\ &- \sin\alpha \sum_{k=1}^{n} \left[\int_{\theta_{ki}}^{\theta_{kj}} (\sin\theta - \sin\theta_0)(\sin\theta - \mu\cos\theta)(A_k Y_k + B_k\rho_{tk} V_{zk}^2 \cos^2\theta)\mathrm{d}\theta \right] \end{aligned} \right) \end{cases}, \tag{9}$$

where the total layers penetrated of target $n = \mathrm{floor}(z\sin\alpha/h)$ and $n \le m$; L_h is the thickness of each layer; A_k and B_k are the constants related to the characteristics of the k layer; Y_k and ρ_{tk} are the yield strength and density of the k layer, respectively; and V_{zk} is the impact velocity of projectile on the k layer.

(2) After the nose wholly penetrates into the target and before it is out through the bottom surface ($L_h < z\sin\alpha \le L_t$), the contact force of the shank in the local coordinate system of projectile can be obtained as:

$$F_{z-\mathrm{shank}} = \sum_{k=\mathrm{floor}\left(\frac{L_h\sin\alpha}{h}\right)+1}^{\mathrm{floor}\left(\frac{(z-L_h)\sin\alpha}{h}\right)} 2a\pi Y_k \mu_k h_k. \tag{10}$$

So the contact force of shank in the global coordinate system of target can be obtained as follows:

$$\begin{cases} F_{z'-\mathrm{shank}} = F_{z-\mathrm{shank}}\sin\alpha \\ F_{x'-\mathrm{shank}} = F_{z-\mathrm{shank}}\cos\alpha. \end{cases} \tag{11}$$

The contact force of projectile of target can be calculated as:

$$\begin{cases} F_{z'} = 2\pi s^2 \left(\begin{array}{l} \sin\alpha \sum\limits_{k=1}^{n} \left[\int\limits_{\theta_{ki}}^{\theta_{kj}} (\sin\theta - \sin\theta_0)(\cos\theta + \mu\sin\theta)(A_k Y_k + B_k \rho_{tk} V_{zk}^2 \cos^2\theta)\mathrm{d}\theta \right] \\ + \cos\alpha \sum\limits_{k=1}^{n} \left[\int\limits_{\theta_{ki}}^{\theta_{kj}} (\sin\theta - \sin\theta_0)(\sin\theta - \mu\cos\theta)(A_k Y_k + B_k \rho_{tk} V_{zk}^2 \cos^2\theta)\mathrm{d}\theta \right] \end{array} \right) \\ \quad + \sum\limits_{k=\mathrm{floor}\left(\frac{L_h \sin\alpha}{h}\right)+1}^{\mathrm{floor}\left(\frac{(z-L_h)\sin\alpha}{h}\right)} 2a\pi Y_k \mu_k h_k \sin\alpha, \\ F_{x'} = 2\pi s^2 \left(\begin{array}{l} \cos\alpha \sum\limits_{k=1}^{n} \left[\int\limits_{\theta_{ki}}^{\theta_{kj}} (\sin\theta - \sin\theta_0)(\cos\theta + \mu\sin\theta)(A_k Y_k + B_k \rho_{tk} V_{zk}^2 \cos^2\theta)\mathrm{d}\theta \right] \\ - \sin\alpha \sum\limits_{k=1}^{n} \left[\int\limits_{\theta_{ki}}^{\theta_{kj}} (\sin\theta - \sin\theta_0)(\sin\theta - \mu\cos\theta)(A_k Y_k + B_k \rho_{tk} V_{zk}^2 \cos^2\theta)\mathrm{d}\theta \right] \end{array} \right) \\ \quad + \sum\limits_{k=\mathrm{floor}\left(\frac{L_h \sin\alpha}{h}\right)+1}^{\mathrm{floor}\left(\frac{(z-L_h)\sin\alpha}{h}\right)} 2a\pi Y_k \mu_k h_k \cos\alpha. \end{cases} \tag{12}$$

(3) Before the nose is wholly out through the target ($L_t < (z\sin\alpha) \le (L_t + L_h) < L$), the contact force of nose in the global coordinate system of target can be obtained as:

$$\begin{cases} F_{z'-\mathrm{nose}} = 2\pi s^2 \left(\begin{array}{l} \sin\alpha \sum\limits_{k=\mathrm{floor}\left(\frac{L_h - z + L_{\mathrm{target}}}{h}\sin\alpha\right)}^{\mathrm{floor}\left(\frac{L_{\mathrm{target}}}{h}\sin\alpha\right)} \left[\int\limits_{\theta_{ki}}^{\theta_{kj}} (\sin\theta - \sin\theta_0)(\cos\theta + \mu\sin\theta)(A_k Y_k + B_k \rho_{tk} V_{zk}^2 \cos^2\theta)\mathrm{d}\theta \right] \\ + \cos\alpha \sum\limits_{k=\mathrm{floor}\left(\frac{L_h - z + L_{\mathrm{target}}}{h}\sin\alpha\right)}^{\mathrm{floor}\left(\frac{L_{\mathrm{target}}}{h}\sin\alpha\right)} \left[\int\limits_{\theta_{ki}}^{\theta_{kj}} (\sin\theta - \sin\theta_0)(\sin\theta \right. \\ \left. - \mu\cos\theta)(A_k Y_k + B_k \rho_{tk} V_{zk}^2 \cos^2\theta)\mathrm{d}\theta \right] \end{array} \right) \\ F_{x'-\mathrm{nose}} = 2\pi s^2 \left(\begin{array}{l} \cos\alpha \sum\limits_{k=\mathrm{floor}\left(\frac{L_h - z + L_{\mathrm{target}}}{h}\sin\alpha\right)}^{\mathrm{floor}\left(\frac{L_{\mathrm{target}}}{h}\sin\alpha\right)} \left[\int\limits_{\theta_{ki}}^{\theta_{kj}} (\sin\theta - \sin\theta_0)(\cos\theta + \mu\sin\theta)(A_k Y_k + B_k \rho_{tk} V_{zk}^2 \cos^2\theta)\mathrm{d}\theta \right] \\ - \sin\alpha \sum\limits_{k=\mathrm{floor}\left(\frac{L_h - z + L_{\mathrm{target}}}{h}\sin\alpha\right)}^{\mathrm{floor}\left(\frac{L_{\mathrm{target}}}{h}\sin\alpha\right)} \left[\int\limits_{\theta_{ki}}^{\theta_{kj}} (\sin\theta - \sin\theta_0)(\sin\theta \right. \\ \left. - \mu\cos\theta)(A_k Y_k + B_k \rho_{tk} V_{zk}^2 \cos^2\theta)\mathrm{d}\theta \right] \end{array} \right). \end{cases} \tag{13}$$

Table 1: Viscoelastic properties of Kevlar/epoxy

E_0 (GPa)	E_1 (GPa)	E_2 (GPa)	η_1 (GPa s)	η_2 (GPa s)	D_0	a	α	β
409	387	351	8.5	16.89	0.70	0.052	−4,321	5,872

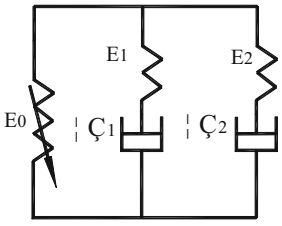

Figure 2: Nonlinear viscoelastic model.

The contact force of shank in the global coordinate system of target can be obtained as:

$$\begin{cases} F_{z'-\text{shank}} = \sum_{k=1}^{\text{floor}\left(\frac{(L_h - z + L_{\text{target}})\sin\alpha}{h}\right)} 2a\pi Y_k \mu_k h_k \sin\alpha, \\ F_{x'-\text{shank}} = \sum_{k=1}^{\text{floor}\left(\frac{(L_h - z + L_{\text{target}})\sin\alpha}{h}\right)} 2a\pi Y_k \mu_k h_k \cos\alpha. \end{cases} \tag{14}$$

So the contact force of the whole projectile can be obtained as:

$$\begin{cases} F_{z'} = F_{z'-\text{nose}} + F_{z'-\text{shank}} \\ F_{x'} = F_{x'-\text{nose}} + F_{x'-\text{shank}}. \end{cases} \tag{15}$$

(4) After the nose penetrates out the target and before the end of shank penetrates into the target ($(L_t + L_h) < (z \sin\alpha) \le L$), the contact force of nose equals to zero, so the contact force of projectile can be calculated as:

$$\begin{cases} F_{z'} = F_{z'-\text{shank}} = F_{z-\text{shank}} \sin\alpha \\ \quad = \sum_{k=1}^{m} 2a\pi Y_k \mu_k h_k \sin\alpha, \\ F_{x'} = F_{x'-\text{shank}} = F_{z-\text{shank}} \cos\alpha \\ \quad = \sum_{k=1}^{m} 2a\pi Y_k \mu_k h_k \cos\alpha. \end{cases} \tag{16}$$

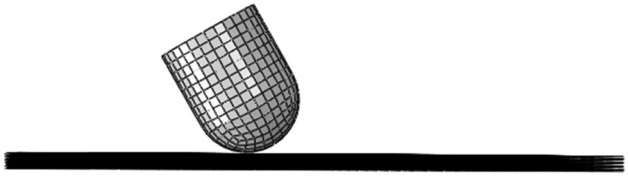

Figure 3: Oblique impact simulation model.

(5) Before the end of the shank penetrates out of the target ($L < (z \sin\alpha) \le (L + L_t)$), some parts of shank stay in the target, so the contact force of projectile can be calculated as:

$$\begin{cases} F_{z'-\text{shank}} = F_{z-\text{shank}} \sin\alpha \\ \quad = \sum_{k=\text{floor}\left(\frac{z-L}{h}\right)}^{m} 2a\pi Y_k \mu_k h_k \sin\alpha, \\ F_{x'-\text{shank}} = F_{z-\text{shank}} \cos\alpha \\ \quad = \sum_{k=\text{floor}\left(\frac{z-L}{h}\right)}^{m} 2a\pi Y_k \mu_k h_k \cos\alpha. \end{cases} \tag{17}$$

(6) After the end of shank penetrates out of the target ($(L + L_t) < (z \sin\alpha)$), the contact force equals to zero.

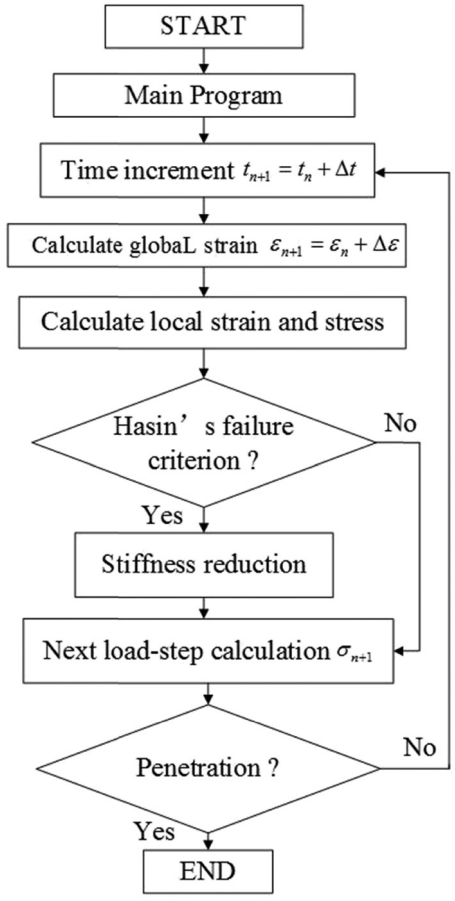

Figure 4: Flow chart of simulation in VUMAT.

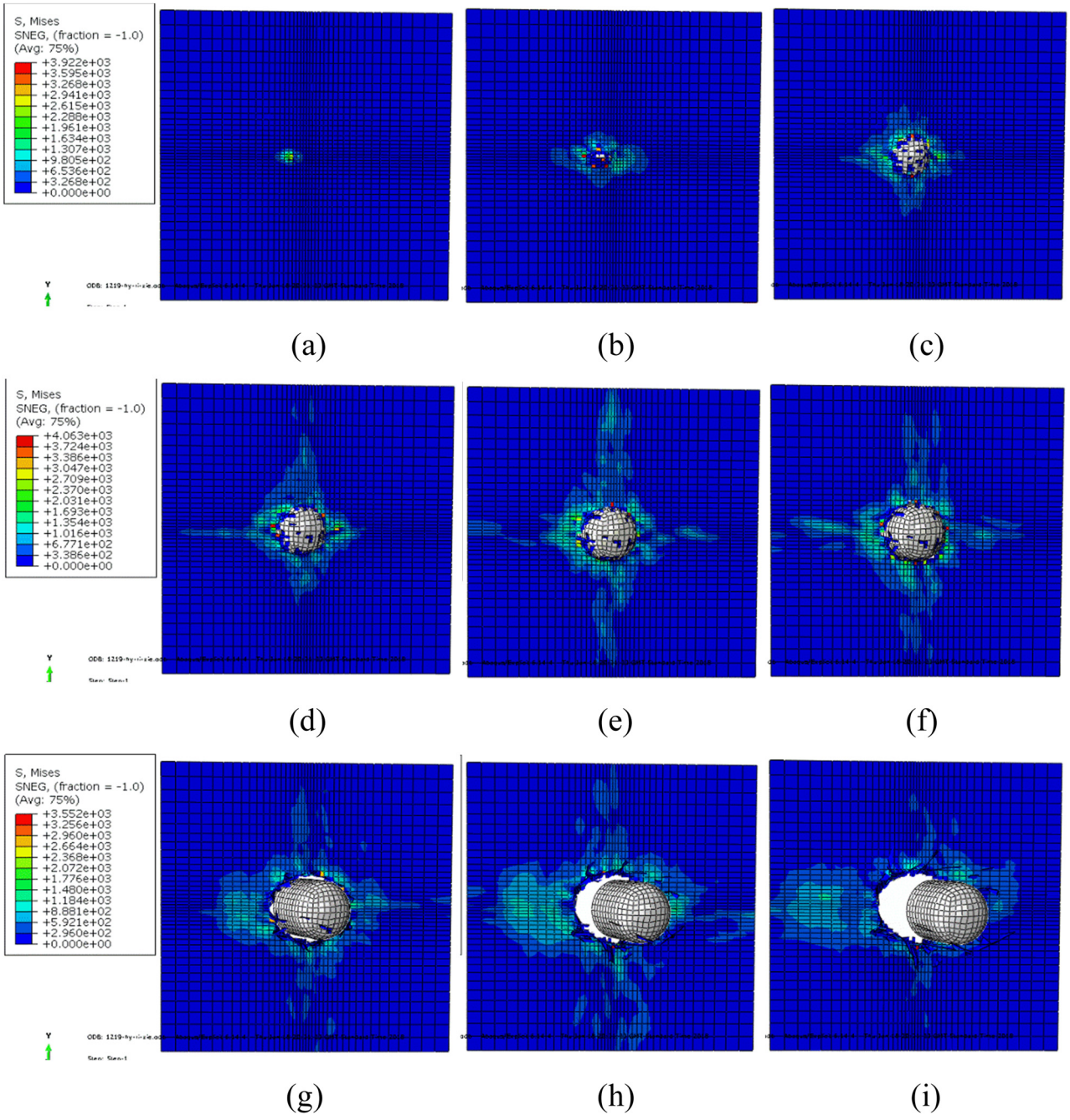

Figure 5: Simulated stress contours of 800 m/s oblique impact: (a) 5 μs, (b) 10 μs, (c) 15 μs, (d) 20 μs, (e) 25 μs, (f) 30 μs, (g) 35 μs, (h) 40 μs, and (i) 45 μs.

3 Mechanical model

3.1 Constitutive model

It has been proved that the epoxy material has a viscoelastic behavior and the Kevlar/epoxy composite presents obviously strain rate-dependent property. The rate-dependent constitutive model of Kevlar fiber was based on a literature work [18], and it is used to investigate impact resistance performance of hybrid composite by employing the VUMAT subroutine of Abaqus.

The two-term nonlinear spring-dashpot system model was employed [19], the constitutive model of Kevlar layers considered damage was investigated, and a new damage factor $D_0\left(\frac{\dot{\varepsilon}}{\dot{\varepsilon}_0}\right)^a$ was proposed, reflecting the

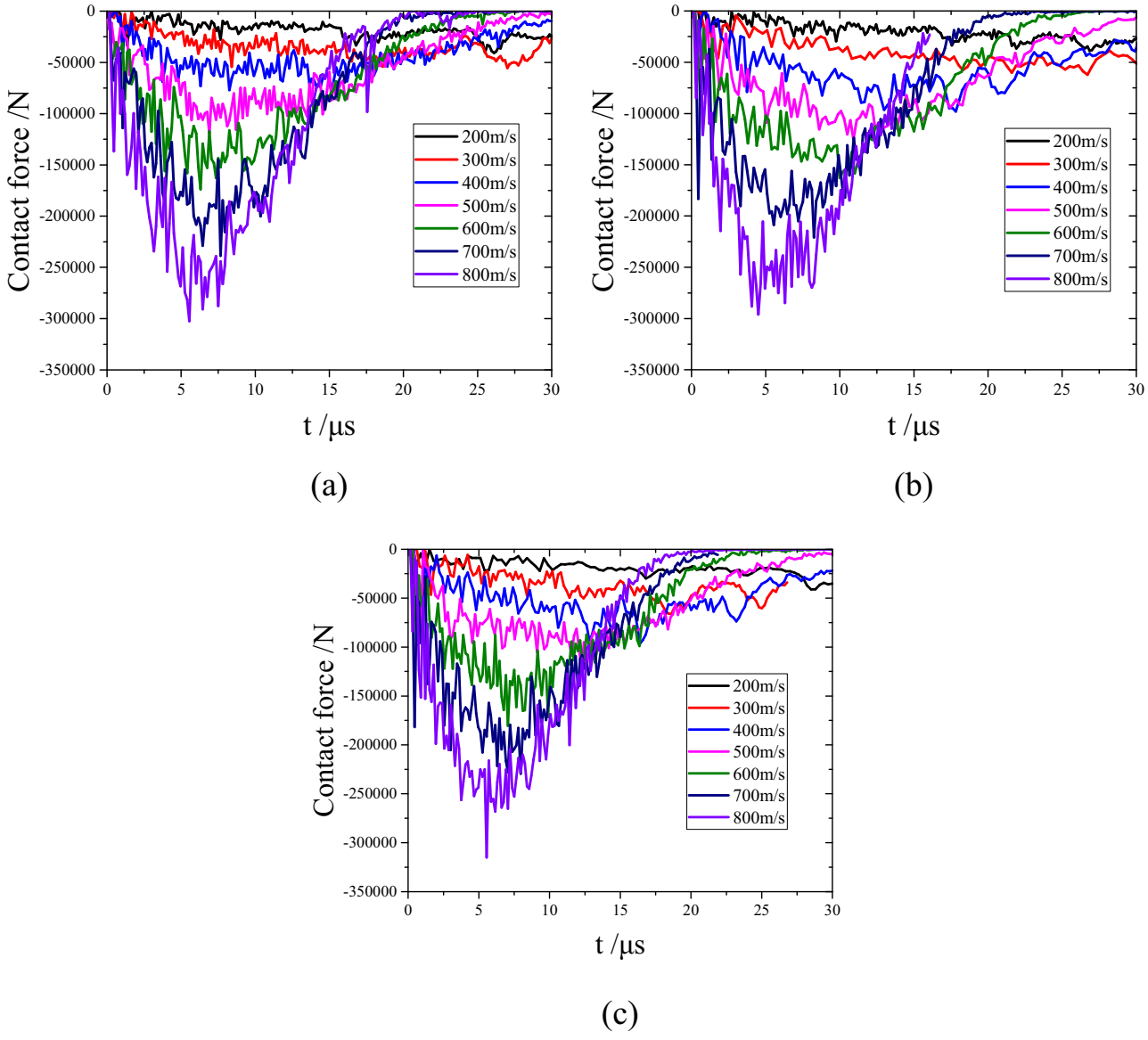

Figure 6: Contact forces of simulation: (a) carbon, (b) Kevlar, and (c) hybrid.

influence from strain rate. The constitutive model was written as follows:

$$\sigma = \left(1 - D_0\left(\frac{\dot{\varepsilon}}{\dot{\varepsilon}_0}\right)^a\right)\left\{E_0\varepsilon + \alpha\varepsilon^2 + \beta\varepsilon^3 + E_1\varphi_1\dot{\varepsilon}\left[1 - \exp\left(-\frac{\varepsilon}{\dot{\varepsilon}\varphi_1}\right)\right] + E_2\varphi_2\dot{\varepsilon}\left[1 - \exp\left(-\frac{\varepsilon}{\dot{\varepsilon}\varphi_2}\right)\right]\right\}, \tag{18}$$

where $\varphi_1 = \frac{\eta_1}{E_1}$, $\varphi_2 = \frac{\eta_2}{E_2}$. The viscoelastic properties of Kevlar/epoxy are shown in Table 1 (Figure 2).

3.2 Failure criterion

Hashin's failure criterion is widely used to predict the failure of component structures, and the failure modes are modified due to the effects from strain rate as follows [20]:

Tensile fiber mode, $\sigma_{11} \geq 0$:

$$\left(\frac{\sigma_{11}}{T_{11}^{\star}}\right)^2 + \lambda\left(\frac{\tau_{12}}{S_{12}^{\star}}\right)^2 + \lambda\left(\frac{\tau_{13}}{S_{13}^{\star}}\right)^2 \geq 1. \tag{19}$$

Compressive fiber mode $\sigma_{11} < 0$:

$$-\frac{\sigma_{11}}{C_{11}^{\star}} \geq 1. \tag{20}$$

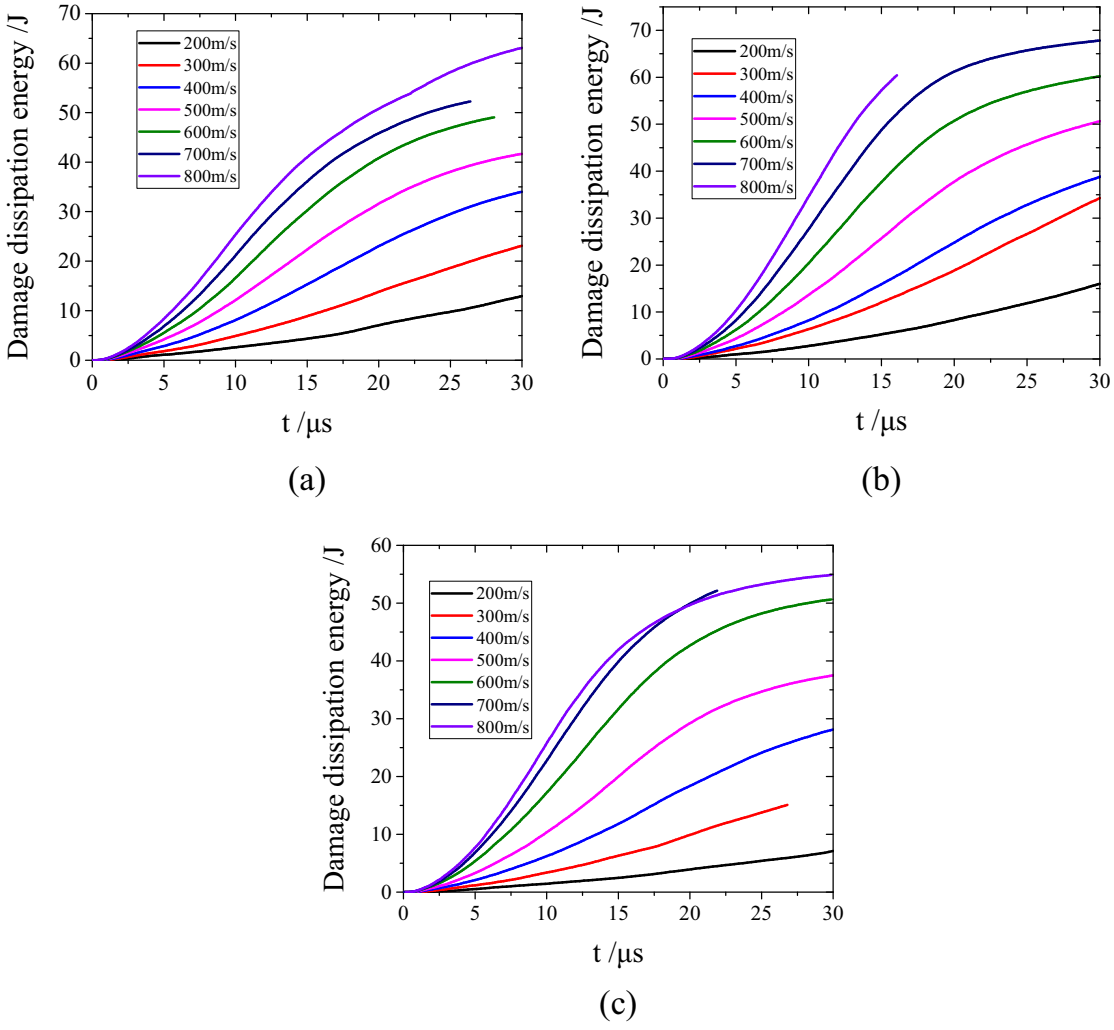

Figure 7: Damage dissipation energy of simulation: (a) carbon, (b) Kevlar, and (c) hybrid.

Tensile matrix mode $\sigma_{22} + \sigma_{33} \geq 0$:

$$\left(\frac{\sigma_{22} + \sigma_{33}}{T_{22}^{\star}}\right)^2 + \frac{\tau_{23}^2 - \sigma_{22}\sigma_{33}}{(S_{23}^{\star})^2} + \frac{\tau_{12}^2 + \tau_{13}^2}{S_{12}^{\star}} \geq 1. \quad (21)$$

Compressive matrix mode $\sigma_{22} + \sigma_{33} < 0$:

$$\left(\frac{\sigma_{22} + \sigma_{33}}{2S_{12}^{\star}}\right)^2 + \frac{(\sigma_{22} + \sigma_{33})^2}{4(S_{23}^{\star})^2} + \frac{\tau_{23}^2 - \sigma_{22}\sigma_{33}}{(S_{23}^{\star})^2} + \frac{\tau_{12}^2 + \tau_{13}^2}{S_{12}^{\star}} \geq 1, \quad (22)$$

where λ is the shear correction factor; $T_{11}^{\star}$ and $C_{11}^{\star}$ are longitudinal tension and compression strengths of unidirectional laminate in the corresponding strain rate, respectively; $T_{22}^{\star}$ and $C_{22}^{\star}$ are transverse tension and compression strengths of unidirectional laminate in the corresponding strain rate, respectively; and $S_{12}^{\star}$, $S_{13}^{\star}$, and $S_{23}^{\star}$ are the shear strengths in the corresponding strain rate, respectively.

4 Simulation

4.1 Simulation model

The oblique impact simulation model of carbon/Kevlar epoxy composite laminate was established, the thickness of target panel was 7.5 mm, the length and width were all 30 mm, carbon and Kevlar layers were alternant and orthogonally layered with [0°/90°], the bullet was rigid, and its radius was 25 mm, which impacted the hybrid composite laminate along 45° with the initial velocity. The target panel was meshed with 30,000 elements, as shown in Figure 3.

Abaqus/explicit subroutines were developed to define some variables and functions, in order to realize the rheological behaviors of Kevlar and hybrid composites, and to reappear the progressive penetration processes of targets on the serial velocity oblique impacts, and the flow chart of simulation is shown in Figure 4.

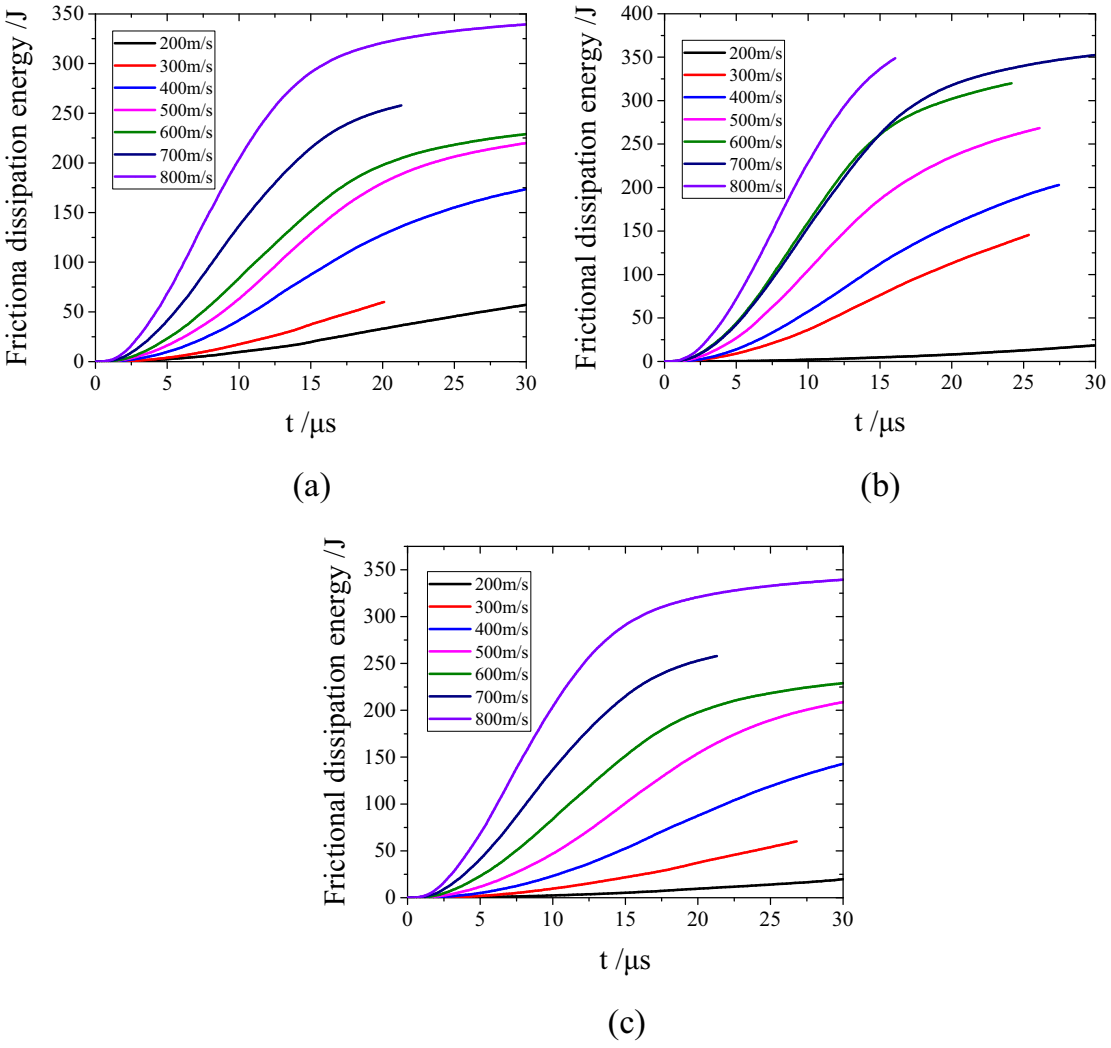

Figure 8: Frictional dissipation energy of simulation: (a) carbon, (b) Kevlar, and (c) hybrid.

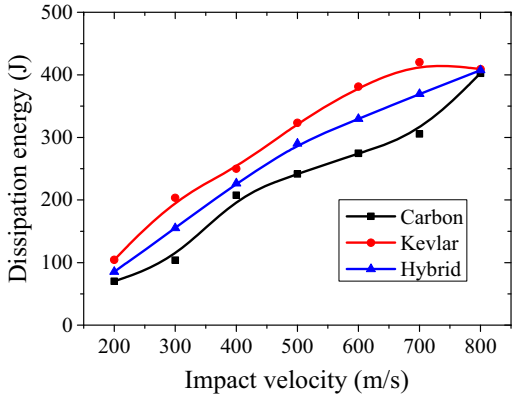

Figure 9: Simulated dissipation energy of composites.

4.2 Simulation results

4.2.1 Stress distribution

The stress and progressive damage of oblique impact were simulated with Abaqus software. When the bullet impacted target first, stress concentration on the contact point appeared (Figure 5a), then the stress contour showed butterfly pattern on the back surface of target (Figure 5b). When the bullet penetrated the bottom of target, the area of high stress expanded and showed cross pattern (Figure 5c–g). When the bullet penetrated the target wholly, the range of stress concentration kept stable (Figure 5h and i).

4.2.2 Contact force

The contact force vs time curves of carbon, Kevlar, and carbon/Kevlar hybrid composite laminates were plotted in different velocities (Figure 6). It showed that contact force of hybrid composite laminate was 11% lower than single composite laminate on the same velocity. That means the hybrid composite reduces the impact velocity effectively.

4.2.3 Damage dissipation energy

The damage dissipation energies of single and hybrid composite laminates on a series of impact velocities were investigated (Figure 7). It showed that damage dissipation energies of hybrid composite laminate were 16.6–40% lower than single composite laminate, and hybrid composite showed excellent damage resistance ability. Carbon/Kevlar hybrid composite combined the high strength of carbon and excellent toughness of Kevlar, so when the bullet impacted the target, the damage dissipation energy was reduced by combined actions from different composites. With the increase in initial impact velocity, the damage dissipation energy increased due to the failure of fibers. In the impact time, the damage dissipation energy showed three-stage non-linear characteristic. At the initial impact, the damage dissipation increased slowly before 5 μs, then it increased rapidly with impact at the range of 5–15 μs, because the most damages occurred in this stage. Increase rate of damage dissipation energy was gentle after 15 μs.

4.2.4 Frictional dissipation energy

The frictional dissipation energy also showed three-stage non-linear trend with impact (Figure 8). It increased rapidly for short time and reached stability in the end. Kevlar composite showed the superior absorption ability, so the hybrid composite target was produced with Kevlar to prevent the penetration.

Total dissipation energy of targets was calculated for different impact velocities (Figure 9). It showed "energy dissipation velocity effect": dissipation energy was increased with the increase in impact velocity.

5 Conclusion

The oblique penetrations of hybrid composite target with bullet on the different velocities were investigated. The contact force of laminate was derived theoretically and plotted from simulation in impact process. The frictional dissipation energy was the action to prevent penetration. Damage and frictional dissipation energies both showed three-stage non-linear trend. Contact force of hybrid composite laminate was 11% lower than single composite laminate on the same velocity. Damage dissipation energies of hybrid composite laminate were 16.6–40% lower than single composite laminate, which showed the excellent damage resistance ability of hybrid composite. The results of this article suggested the design of engine case.

Funding information: This work was partially supported by National Natural Science Foundation of China (Grant No. 12102152) and State Key Laboratory of Mechanics and Control of Mechanical Structures (Nanjing University of Aeronautics and Astronautics) (Grant No. MCMS-E-0221Y02).

Conflict of interest: Authors state no conflict of interest.

References

[1] Sayer M, Bektas NB, Sayman O. An experimental investigation on the impact behavior of hybrid composite plates. Compos Struct. 2010;92(5):1256–62.
[2] Heydari-Meybodi M, Saber-Samandari S, Sadighi M. A new approach for prediction of elastic modulus of polymer/nanoclay composites by considering interfacial debonding: experimental and numerical investigations. Compos Sci Technol. 2015 Sept 29;117:379–85.
[3] Xu MM, Huang GY, Dong YX, Feng SS. An experimental investigation into the high velocity penetration resistance of CFRP and CFRP/aluminium laminates. Compos Struct. 2018 Mar 15;188:450–60.
[4] Naresh K, Shankar K, Rao BS, Velmurugan R. Effect of high strain rate on glass/carbon/hybrid fiber reinforced epoxy laminated composites. Compos B Eng. 2016 Sept 1;100:125–35.
[5] Tirillo J, Ferrante L, Sarasini F, Lampani L, Barbero E, Sanchez-Saez S, et al. High velocity impact behaviour of hybrid basalt-carbon/epoxy composites. Compos Struct. 2017 May 15;168:305–12.
[6] Xie WH, Meng SH, Ding L, Jin H, Han GK, Wang LB, et al. High velocity impact tests on high temperature carbon-carbon composites. Compos B Eng. 2016 Aug 1;98:30–8.
[7] Tao C, Qiu J, Yao W, Ji H. A novel method for fatigue delamination simulation in composite laminates. Compos Sci Technol. 2016 May 18;128:104–15.
[8] Yao L, Yu H, Wang C, He W. Numerical and experimental investigation on the oblique successive impact behavior and accumulated damage characteristics of fiber metal laminates. Thin-wall Struct. 2021;166:108033.
[9] Srivatsava M, Rama Sreekanth PS. Experimental characterization of dynamic mechanical properties of hybrid carbon-

Kevlar reinforced composite with sandwich configuration. Mater Today. 2020;27(2):931–5.
[10] Woo SC, Kim TW. High strain-rate failure in carbon/Kevlar hybrid woven composites via a novel SHPB-AE coupled test. Compos B Eng. 2016 July 15;97:317–28.
[11] Sanchez-Galvez V, Galvez F, Sancho R, Cendon D. A new analytical model to simulate high-speed impact onto composite materials targets. Int J Impact Eng. 2017;108:322–33.
[12] Sanchez-Galvez V, Sanchez Paradela L, Galvez F. Analytical simulation of high-speed impact onto hybrid glass/carbon epoxy composites targets. Proc Eng. 2014;88:101–8.
[13] Kong X, Fang Q, Wu H, Zhang Y. Finite spherical cavity expansion method for layering effect. Acta Mech Solid Sin. 2016;29(6):642–54.
[14] Meng C, Tan Q, Jiang Z, Song D, Liu F. Approximate solutions of finite dynamic spherical cavity-expansion models for penetration into elastically confined concrete targets. Int J Impact Eng. 2018;114:182–93.
[15] Chen HC, Chen YL, Shen BC. Ballistic resistance analysis of double-layered composite material structures. Theor Appl Fract Mec. 2012;62:15–25.
[16] Forrestal MJ, Okajima K, Luk VK. Penetration of 6061-T651 aluminum targets with rigid long rods. J Appl Mech. 1988;55:755–60.
[17] Luc VK, Forrestal MJ, Amos DE. Dynamic spherical cavity-expansion of strain-hardening targets. J App Mech. 1998;55:755–60.
[18] Karim M. Constitutive modeling and failure criteria of carbon-fiber reinforced polymers under high strain rates. America: The University of Akron; 2005.
[19] Lili W, Zhiping T, Yongchi L. Progress on impact dynamics. China: University of Science and technology Press of China; 1992. Chinese.
[20] Gu J, Chen P. Some modifications of Hashin's failure criteria for unidirectional composite materials. Compos Struct. 2017 Dec 15;182:143–52.